PHYSICAL REVIEW E **93**, 013308 (2016)

Lattice Boltzmann modeling of three-phase incompressible flows

H. Liang,[1] B. C. Shi,[2,3,*] and Z. H. Chai[2,3]
[1]*Department of Physics, Hangzhou Dianzi University, Hangzhou 310018, China*
[2]*School of Mathematics and Statistics, Huazhong University of Science and Technology, Wuhan, 430074, China*
[3]*State Key Laboratory of Coal Combustion, Huazhong University of Science and Technology, Wuhan 430074, China*

(Received 29 September 2015; revised manuscript received 20 December 2015; published 20 January 2016)

In this paper, based on multicomponent phase-field theory we intend to develop an efficient lattice Boltzmann (LB) model for simulating three-phase incompressible flows. In this model, two LB equations are used to capture the interfaces among three different fluids, and another LB equation is adopted to solve the flow field, where a new distribution function for the forcing term is delicately designed. Different from previous multiphase LB models, the interfacial force is not used in the computation of fluid velocity, which is more reasonable from the perspective of the multiscale analysis. As a result, the computation of fluid velocity can be much simpler. Through the Chapman-Enskog analysis, it is shown that the present model can recover exactly the physical formulations for the three-phase system. Numerical simulations of extensive examples including two circular interfaces, ternary spinodal decomposition, spreading of a liquid lens, and Kelvin-Helmholtz instability are conducted to test the model. It is found that the present model can capture accurate interfaces among three different fluids, which is attributed to its algebraical and dynamical consistency properties with the two-component model. Furthermore, the numerical results of three-phase flows agree well with the theoretical results or some available data, which demonstrates that the present LB model is a reliable and efficient method for simulating three-phase flow problems.

DOI: 10.1103/PhysRevE.93.013308

I. INTRODUCTION

Multicomponent flows frequently arise in many important engineering and scientific applications. A typical example in this regard is enhanced oil recovery, which involves at least three-phase fluids including oil, water, and air [1]. Another example is the proton exchange membrane fuel cell, where hydrogen reacts chemically with oxygen in the catalyst layer and generates the water vapor. Then the transport of a fluid system containing hydrogen, oxygen, water in the diffusion layer, and a gas microchannel is a dramatic three-component flow [2]. Oftentimes these flows are also encountered in microfluidic devices [3], where multispecies droplet generation, coalescence, or breakup takes place. The theoretical analysis on these flows is rather tough and challenging since it involves complex interactions among multiple fluids and solid materials, and experimental studies may be restricted due to expensive costs and arbitrarily changed setups. With the rapid development of the computer technology, numerical modeling plays a significant role in studying three-phase flows, and many researchers have made an effort to construct efficient numerical approaches for simulating three-phase flows, such as the level set [4–6], front-tracking [7], volume of fluid [8], smoothed particle hydrodynamics [9], and phase field [10–15] methods.

The lattice Boltzmann (LB) method, as an alternative simulation technique, has received great success in modeling both fluid dynamics [16,17] and nonlinear equation systems [18–22]. Different from the traditional numerical methods, the LB method is suitable for parallel computation and easy to treat complicated boundary conditions. Additionally, the microscopic interactions between fluids can be incorporated straightforwardly in the LB method such that multiphase flows can be simulated effectively [16,17]. Up to now, several types of LB models for multiphase flows have been established under different physical pictures of the interactions, which can be commonly classified into four categories: the color model [23], the pseudopotential model [24–28], the free-energy model [29,30], and the phase-field-based model [31–37]. In succession, a large number of successful applications of these models to multiphase systems have also been reported [38–40]. However, almost all models are able to deal only with two-phase systems, and relatively little attention has been paid to the modeling of multiphase flows with three or more fluids. Halliday *et al.* [41,42] introduced a color gradient for each of fluid-fluid interfaces in the color model such that continuum multicomponent flows can be simulated. Due to the numerical instability problem, however, their models are limited to density-matched fluids where the Boussinesq approximation holds. To simulate multicomponent flows with density contrast, Leclaire *et al.* [43] developed a LB model based on the improved color-gradient model [44], where three subcollision operators are incorporated in their model, and to improve numerical stability, a high-order discrete operator is also used for the calculation of the color gradient. Recently the widely used pseudopotential model [24,25] was also extended to simulate multicomponent flows by introducing the interaction among three fluids [45], while it is not clear whether the model can recover the correct macroscopic equations [46]. On the other hand, it is known that the phase-field theory can provide a firm foundation on the interface physics such that interface dynamics can be well described, while to the authors' knowledge, there is no available work on the construction of LB model for three-phase flows based on the phase-field theory.

In this paper, we propose an alternative LB model for three-phase flows based on the multicomponent phase-field

---

[*] shibc@hust.edu.cn

theory. The proposed model has some distinct features. First, the model utilizes two LB equations to track the interfaces among three phases, where some proper source terms on time derivative are incorporated to derive the correct interfacial equations. Second, due to the elaborate choice of bulk free energy [12,14], the present model coincides exactly with the diphasic phase-field model when one component vanishes. Third, different from some previous LB models [36,47,48], a novel distribution function for the forcing term is delicately designed and incorporated into the LB equation for flow field such that the Navier-Stokes (NS) equations can be recovered correctly. In addition, the interfacial force is not used to shift the macroscopic velocity, and the computation then is much simpler.

The rest of this paper is organized as follows. In Sec. II, we present a brief introduction to multicomponent phase field theory. Then the developed LB model for three-phase flow systems is given in Sec. III, where the Chapman-Enskog (CE) analysis is also conducted to match the NS equations. In Sec. IV, we perform a series of numerical experiments to test the performance of the model. Finally, a brief summary is given in Sec. V.

II. MULTICOMPONENT PHASE-FIELD THEORY

The phase-field method is a special class of diffuse-interface models that has become more and more popular for modeling multiphase flows [49–51]. In this work, we consider an incompressible system constituting three immiscible Newtonian fluids. Three order parameters denoted by c_1, c_2, and c_3 are introduced to describe this ternary system, and each of them represents the volume fraction of one fluid within the mixture. The values of these order parameters cannot be arbitrarily chosen, and they are linked through the constraint [12–14]

$$\sum_{i=1}^{3} c_i = 1, 0 \leqslant c_i \leqslant 1. \tag{1}$$

Denoting the flow domain by Ω, one can postulate the free energy of a three-phase system as [12,14]

$$\Psi = \int_{\Omega} \left[\frac{12}{D} F(c_1,c_2,c_3) + \sum_{i=1}^{3} \frac{3}{8} D\lambda_i |\nabla c_i|^2 \right] d\Omega, \tag{2}$$

where $F(c_1,c_2,c_3)$ is the bulk free energy to be determined later, D is a characteristic scale of the interface thickness, and λ_i are physical parameters related to the surface tensions. In the phase-field theory, the time evolution of the phase function c_i is described by its advection with the fluid velocity, and the gradient of the free energy which can be taken in $H^{-1}(\Omega)$ [49,51]. However, in order to satisfy the conservation (1), a Lagrangian multiplier β should be introduced into the gradient term on the free energy [12,13]. Then the system of equations can be written as

$$\frac{\partial c_i}{\partial t} + \nabla \cdot c_i \mathbf{u} = \nabla \cdot (M_i \nabla \mu_i), \qquad i = 1,2,3, \tag{3}$$

where M_i is a mobility, and μ_i is the chemical potential given by

$$\mu_i = \frac{\partial \Psi}{\partial c_i} + \beta = \frac{12}{D}\frac{\partial F}{\partial c_i} - \frac{3}{4} D\lambda_i \nabla^2 c_i + \beta, \qquad i = 1,2,3. \tag{4}$$

Now we give details on how to derive the expression of β. Summing Eq. (3) over i and denoting the variable $S = c_1 + c_2 + c_3$, we can easily derive the following equation:

$$\frac{\partial S}{\partial t} + \nabla \cdot S\mathbf{u} = \nabla \cdot M_0 \nabla \left(-\frac{3}{4} D \nabla^2 S + \sum_{i=1}^{3} \frac{12}{D\lambda_i}\frac{\partial F}{\partial c_i} + \beta \sum_{i=1}^{3} \frac{1}{\lambda_i} \right), \tag{5}$$

where the condition $M_1\lambda_1 = M_2\lambda_2 = M_3\lambda_3 = M_0$ has been enforced [12]. Because of the conservation (1), $S = 1$ should be the solution of Eq. (5), and we can ultimately derive the Lagrangian multiplier β as

$$\beta = -\sum_{i=1}^{3} \frac{4\lambda_T}{D\lambda_i}\frac{\partial F}{\partial c_i}, \tag{6}$$

where λ_T is defined by

$$\frac{3}{\lambda_T} = \sum_{i=1}^{3} \frac{1}{\lambda_i}. \tag{7}$$

Based on Eq. (6), the Cahn-Hilliard (CH) phase equations for the three-component system can be recast as

$$\frac{\partial c_i}{\partial t} + \nabla \cdot c_i \mathbf{u} = \nabla \cdot \left(\frac{M_0}{\lambda_i} \nabla \mu_i \right) \tag{8}$$

with

$$\mu_i = \frac{4\lambda_T}{D} \sum_{j\neq i} \left[\frac{1}{\lambda_j} \left(\frac{\partial F}{\partial c_i} - \frac{\partial F}{\partial c_j} \right) \right] - \frac{3}{4} D\lambda_i \nabla^2 c_i, \quad i = 1,2,3. \tag{9}$$

Supposing the physical parameters D and M_0 being fixed, the system of Eq. (8) then can be completely determined once the bulk free energy F and the coefficients λ_i are given. Up to now, several researchers [10–14] have given theoretical analyses of the choice of the bulk free energy. In this work, the one reported in Refs. [12,14] is adopted in that the model can be well posed and also preserves algebraical and dynamical consistency properties with the diphasic systems when one component vanishes. Following Refs. [12,14], the expression of the bulk free energy F can be presented as

$$F(c_1,c_2,c_3) = F_0(c_1,c_2,c_3) + \lambda c_1^2 c_2^2 c_3^2 \times [\varphi(c_1) + \varphi(c_2) + \varphi(c_3)], \tag{10}$$

where λ is a non-negative parameter, and $F_0(c_1,c_2,c_3)$ is given by

$$F_0(c_1,c_2,c_3) = \frac{\lambda_1}{2} c_1^2 (1-c_1)^2 + \frac{\lambda_2}{2} c_2^2 (1-c_2)^2 + \frac{\lambda_3}{2} c_3^2 (1-c_3)^2, \tag{11}$$

where the coefficients λ_i are related to the surface tensions,

$$\begin{aligned}\lambda_1 &= \sigma_{12}+\sigma_{13}-\sigma_{23},\\ \lambda_2 &= \sigma_{12}+\sigma_{23}-\sigma_{13},\\ \lambda_3 &= \sigma_{13}+\sigma_{23}-\sigma_{12},\end{aligned} \tag{12}$$

where λ_i $(i=1,2,3)$ is a positive parameter, and σ_{12}, σ_{13}, and σ_{23} represent the surface tension between two fluids of a three-phase system. Here φ in Eq. (10) is the function $\varphi(x)=\frac{1}{(1+x^2)^\alpha}$, where α varies between 0 and 1 for the two-dimensional flows and changes from 0 to $\frac{8}{17}$ for the three-dimensional case. Without loss of generality, we fix the parameter α to be 0 in this work. Finally, we would like to point out that using the conservation (1), the system of equations reduce to a set of two coupled CH phase equations, which will be used for the construction of LB model. In a similar way, it is easily to derive the relationship among three chemical potentials:

$$\sum_{i=1}^{3}\frac{\mu_i}{\lambda_i}=0. \tag{13}$$

To describe the fluid flows, the CH phase equations should be coupled with the NS equations with surface tension force, which can be written as [36,49–51]

$$\nabla\cdot\mathbf{u}=0, \tag{14a}$$

$$\rho\left(\frac{\partial\mathbf{u}}{\partial t}+\mathbf{u}\cdot\nabla\mathbf{u}\right)=-\nabla p+\nabla\cdot[\nu\rho(\nabla\mathbf{u}+\nabla\mathbf{u}^T)] +\mathbf{F}_s+\mathbf{G}, \tag{14b}$$

where ρ is the fluid density, p is the pressure, ν is the kinematic viscosity, $\mathbf{F}_s=\sum_{i=1}^{3}\mu_i\nabla c_i$ is the surface tension force [12], and $\mathbf{G}$ is the external force.

III. LB MODEL FOR THREE-PHASE FLUID FLOWS

A. LB model for three-component CH equations

Due to the conservation $c_1+c_2+c_3=1$, one needs only two LB equations to capture the interfaces among three-phase fluids. The LB equations with the BGK collision operator for the interface tracking are proposed as

$$\begin{aligned} f_k^i(\mathbf{x}+\mathbf{e}_k\delta_t,t+\delta_t)-f_k^i(\mathbf{x},t)\\ =-\frac{1}{\tau_i}[f_k^i(\mathbf{x},t)-f_k^{i,eq}(\mathbf{x},t)]+\delta_t F_k^i(\mathbf{x},t),\end{aligned} \tag{15}$$

where the superscript $i=1$ or 2 denotes the 1-phase or 2-phase, $f_k^i(\mathbf{x},t)$ is the distribution function for the order parameter c_i, $f_k^{i,eq}(\mathbf{x},t)$ is its corresponding equilibrium state, τ_i is a nondimensional relaxation time for the c_i field, δ_t is the time increment. To derive the correct three-component CH equations, a linear equilibrium distribution function $f_k^{i,eq}$ can be introduced as [33,36]

$$f_k^{i,eq}=\begin{cases} c_i+(\omega_k-1)\eta\mu_i, & k=0\\ \omega_k\eta\mu_i+\omega_k c_i\frac{\mathbf{e}_k\cdot\mathbf{u}}{c_s^2}, & k\neq 0,\end{cases} \tag{16}$$

where ω_k and $\mathbf{e}_k$ are weighting coefficient and discrete velocity, and they depend on the choice of lattice model, and η is a free parameter that can be used to adjust the value of the mobility. For the D2Q9 lattice model adopted in this work, ω_k are set as $\omega_0=4/9$, $\omega_{1-4}=1/9$, and $\omega_{5-8}=1/36$, and $\mathbf{e}_k$ can be given by

$$\mathbf{e}_k=\begin{cases}(0,0)c, & k=0,\\ (\cos[(k-1)\pi/2],\sin[(k-1)\pi/2])c, & k=1-4,\\ \sqrt{2}(\cos[(k-5)\pi/2+\pi/4],\sin[(k-5)\pi/2+\pi/4])c, & k=5-8,\end{cases} \tag{17}$$

where $c=\delta_x/\delta_t$ is the lattice speed with δ_x being the grid spacing. Note that the parameter c_s in Eq. (16) is the sound speed satisfying $c_s=c/\sqrt{3}$. By convention, δ_x and δ_t are both normalized and set to be unity.

To recover the CH phase equations without any artificial terms, a proper source term is incorporated in the LB evolution equation, which can be defined as [36]

$$F_k^i=\left(1-\frac{1}{2\tau_i}\right)\frac{\omega_k\mathbf{e}_k\cdot\partial_t c_i\mathbf{u}}{c_s^2}. \tag{18}$$

In this model, the order parameter c_i can be calculated by taking the zeroth moment of the order distribution function

$$c_i=\sum_k f_k^i \tag{19}$$

for $i=1,2$. Because of the conservation, the order parameter c_3 can be derived based on the relation $c_3=1-c_1-c_2$. For simplicity, the fluid density can be determined by the linear interpolation of three order parameters [13],

$$\rho=c_1\rho_1+c_2\rho_2+c_3\rho_3, \tag{20}$$

where ρ_i $(i=1,2,3)$ represents the density of the i phase. We recall the CE analysis technique in order to demonstrate the consistency of the LB evolution equation (15) to the CH phase equations (8). Similar discussion can also be found in Refs. [36,37]. Based on the CE analysis, one can find that the CH phase equations can be recovered correctly from the present model, and the relationship between the mobility M_i and the relaxation factor can also be derived as

$$M_i=\eta c_s^2(\tau_i-0.5)\delta t,\qquad i=1,2. \tag{21}$$

Note that if the parameter η vanishes in Eq. (16), and for the situation with very small mobility, the dimensionless relaxation time τ_i would be close to 0.5, which may cause instability of the LB method and bring some large errors. However, an additional free parameter η introduced in Eq. (16)

can provide much more potential in coping with this case, while without increasing any computational cost.

B. LB model for the NS equations

To complete the modeling of three-phase incompressible flows, the multicomponent CH system should be coupled with the NS equations. In this section, we will develop a LB model for the NS equations with surface tension force. This LB model for the NS equations follows our previous work on the two-phase case [36], and a remarkable difference between them lies in that one must take into consideration of the capillary forces among three-phase fluids here. The LB evolution equation with a source term for the NS equations can be written as [52]

$$\begin{aligned} g_k(\mathbf{x}+\mathbf{e}_k\delta_t,t+\delta_t) - g_k(\mathbf{x},t) \\ = -\frac{1}{\tau_g}[g_k(\mathbf{x},t) - g_k^{eq}(\mathbf{x},t)] + \delta_t G_k(\mathbf{x},t), \end{aligned} \tag{22}$$

where $g_k(\mathbf{x},t)$ is the particle distribution function for fluid field, $g_k^{eq}(\mathbf{x},t)$ is the corresponding equilibrium state, τ_g is a dimensionless relaxation time related to the fluid kinematic viscosity, and $G_k(\mathbf{x},t)$ is the distribution function for the total force. To recover the continuity equation correctly, the equilibrium distribution function g_k^{eq} is delicately designed as [36]

$$g_k^{eq} = \begin{cases} \frac{p}{c_s^2}(\omega_k - 1) + \rho s_k(\mathbf{u}), & k = 0, \\ \frac{p}{c_s^2}\omega_k + \rho s_k(\mathbf{u}), & k \neq 0, \end{cases} \tag{23}$$

where

$$s_k(\mathbf{u}) = \omega_k\left[\frac{\mathbf{e}_k\cdot\mathbf{u}}{c_s^2} + \frac{(\mathbf{e}_k\cdot\mathbf{u})^2}{2c_s^4} - \frac{\mathbf{u}\cdot\mathbf{u}}{2c_s^2}\right]. \tag{24}$$

Different from the previous LB models [36,47,48], a novel distribution function for the forcing term is defined as

$$\begin{aligned} G_k = \left(1 - \frac{1}{2\tau_g}\right)(\mathbf{e}_k - \mathbf{u})\cdot\left[s_k(\mathbf{u})\nabla\rho + (s_k(\mathbf{u}) + \omega_k)\frac{\mathbf{F}}{c_s^2}\right] \\ + \frac{\omega_k \mathbf{e}_k\cdot\mathbf{F}_a}{c_s^2}, \end{aligned} \tag{25}$$

where **F** is the total force and is composed of two parts:

$$\mathbf{F} = \mathbf{F}_s + \mathbf{G}. \tag{26}$$

Here $\mathbf{F}_s$ represents the surface tension force arising from the interaction at interfaces among three fluids, **G** is the body force. To derive the correct momentum equation, an additional interfacial force $\mathbf{F}_a$ is introduced in Eq. (25), which is defined by

$$\mathbf{F}_a = \mathbf{u}[(\rho_1 - \rho_3)\nabla\cdot(M_1\nabla\mu_1) + (\rho_2 - \rho_3)\nabla\cdot(M_2\nabla\mu_2)]. \tag{27}$$

It is clearly seen that this additional term is nonzero in the interfacial region when the densities of three fluids do not equal to each other. This force term is very small in theory, but its effect can be significant at a higher fluid velocity [47]. To incorporate these force effects, the fluid velocity should be computed by

$$\mathbf{u} = \frac{1}{\rho}\left[\sum_k \mathbf{e}_k g_k + 0.5\delta_t(\mathbf{F}_s + \mathbf{G})\right], \tag{28}$$

where the interfacial force $\mathbf{F}_a$ is not included, while it has been used to shift the macroscopic velocity in the previous LB models [36,47,48]. We would like to point out that the former is more reasonable since this force has an order of $O(\epsilon^2)$ from the viewpoint of the CE analysis, where ϵ is a small expansion parameter. Additionally, the pressure can be computed in a particular form [36]:

$$p = \frac{c_s^2}{(1-\omega_0)}\left[\sum_{k\neq 0} g_k + \frac{\delta_t}{2}\mathbf{u}\cdot\nabla\rho + \rho s_0(\mathbf{u})\right]. \tag{29}$$

We also conducted the CE analysis on the LB equation (22), and the details can be consulted in Appendix. The results show that the present model can recover correctly the NS equations with the following kinematic viscosity:

$$\nu = c_s^2(\tau_g - 0.5)\delta_t. \tag{30}$$

In the implementation of the present model, one needs to choose some suitable difference schemes to discretize the derivative terms. Following Refs. [20,53], the following explicit difference scheme is adopted for computing the time derivative in Eq. (18):

$$\partial_t\chi(\mathbf{x},t) = \frac{\chi(\mathbf{x},t) - \chi(\mathbf{x},t-\delta_t)}{\delta_t}, \tag{31}$$

and the widely used isotropic central schemes are applied to calculate the gradient and the Laplacian operator [54,55]:

$$\nabla\chi(\mathbf{x},t) = \sum_{k\neq 0}\frac{\omega_k\mathbf{e}_k\chi(\mathbf{x}+\mathbf{e}_k\delta_t,t)}{c_s^2\delta_t} \tag{32}$$

and

$$\nabla^2\chi(\mathbf{x},t) = \sum_{k\neq 0}\frac{2\omega_k[\chi(\mathbf{x}+\mathbf{e}_k\delta_t,t) - \chi(\mathbf{x},t)]}{c_s^2\delta_t^2}. \tag{33}$$

In the above equations, χ represents an arbitrary variable. It should be noted that the schemes (32) and (33) not only have a secondary-order accuracy in space, but also can ensure the global mass conservation of a multiphase system [55].

At the end of this section, we would like to give some remarks on our model. If all the physical parameters λ_i $(i = 1,2,3)$ are positive and further satisfy $\lambda_i > \frac{\lambda_T}{2}$, the system with the bulk free energy $F = F_0$ not only can be well posed but also can be algebraically and dynamically consistent with the diphasic case [12,14]. So this simple choice $F = F_0$ is acceptable and will be adopted in most of our numerical simulations. Substituting $F = F_0$ into Eq. (9), one can simplify the chemical potentials as

$$\begin{aligned} \mu_i = \frac{12}{D}[\lambda_i c_i(1-c_i)(1-2c_i) - 2\lambda_T c_1 c_2(1-c_1-c_2)] \\ - \frac{3}{4}D\lambda_i\nabla^2 c_i,\ i = 1,2, \end{aligned} \tag{34}$$

and μ_3 can be derived by Eq. (13). If the condition $\lambda_i > \frac{\lambda_T}{2}$ is not satisfied, the system with the bulk free energy $F = F_0$

could not be dynamically consistent [12]. Then the high-order bulk free energy Eq. (10) will be adopted, where the parameter λ should be taken as a positive value. It is noted that in most of previous works [10,11], the bulk free energy is chosen as $F = \sigma_{12}c_1^2c_2^2 + \sigma_{13}c_1^2c_3^2 + \sigma_{23}c_2^2c_3^2$, which does not conform to the corresponding diphasic system, and it will lead to some unphysical behaviors. In addition, different from the previous LB models [36,47,48], the interfacial force $\mathbf{F}_a$ is not applied in the calculation of the macroscopic velocity, which not only seems more reasonable based on the CE analysis, but also makes the computation of the fluid velocity much simpler. Finally, the miscibility properties of the flow components can be described through the free energy. The present model deals only with immiscible ternary fluids, and the extension to the miscible case can be conducted when the free energy is a convex function of the components [56].

IV. NUMERICAL RESULTS AND DISCUSSIONS

In this section, we will validate the proposed LB model through some numerical tests. The tests include two parts. In the first part, an interface-capturing benchmark problem of two circular interfaces is considered, where only the evolution equation (15) is utilized since the velocity field has been prescribed. In the second part, the present LB model will be used to study some basic three-phase flows including the ternary spinodal decomposition, spreading of a liquid lens, and Kelvin-Helmholtz instability, where a detailed comparison between present results and the theoretical results or some available data is also conducted. Here we would like to point out that the grid resolution has been tested, and it has been demonstrated that the present grids used in our work are adequately accurate to give grid-independent results.

A. Circular interface

A basic test of two circular disks is first performed to verify the present LB model for the interface capturing. The initial setup is given as follows. Two circular disks with radius $R = 20$ are placed in a $N_x \times N_y = 200 \times 100$ lattice domain with periodic boundary conditions in both x and y directions. The centers of these disks are located at $(x_{c_1}, y_c) = (50,50)$ and $(x_{c_2}, y_c) = (150,50)$, respectively. For this problem, the initial profiles of the order parameters are expressed as

$$c_1(x,y) = 0.5 + 0.5\tanh\left[2\frac{R - (x - x_{c_1})^2 + (y - y_c)^2}{D}\right],$$
$$c_2(x,y) = 0.5 + 0.5\tanh\left[2\frac{R - (x - x_{c_2})^2 + (y - y_c)^2}{D}\right], \quad (35)$$

where the interface thickness D is fixed at 4.0, the c_3 field is determined by the conservation (1), and the velocity field is fixed to be $\mathbf{u} = 0$. Some other physical parameters in our simulations are set as $\sigma_{12} = \sigma_{13} = \sigma_{23} = 0.1$, $\tau_1 = \tau_2 = 0.8$, and $M_0 = 0.001$. Figure 1 depicts the steady distributions of three order parameters obtained by the present LB method with the current bulk free energy $F = F_0$ and the previous one $F = \sigma_{12}c_1^2c_2^2 + \sigma_{13}c_1^2c_3^2 + \sigma_{23}c_2^2c_3^2$ [10,11]. It can be seen that the present LB scheme with the bulk free energy $F = F_0$ can preserve the exact profiles of order parameters with initial configurations, while there are produced some artificial apparitions of the phase represented by c_1 or c_2 in other phase boundaries. So we can say that the current bulk free energy is a better choice in capturing the interfaces among three-component fluids. To further give a detailed comparison, we also plotted the order distributions along the horizontal center line ($y = N_y/2$) in Figs. 2(a) and 2(b). From Fig. 2(a), we

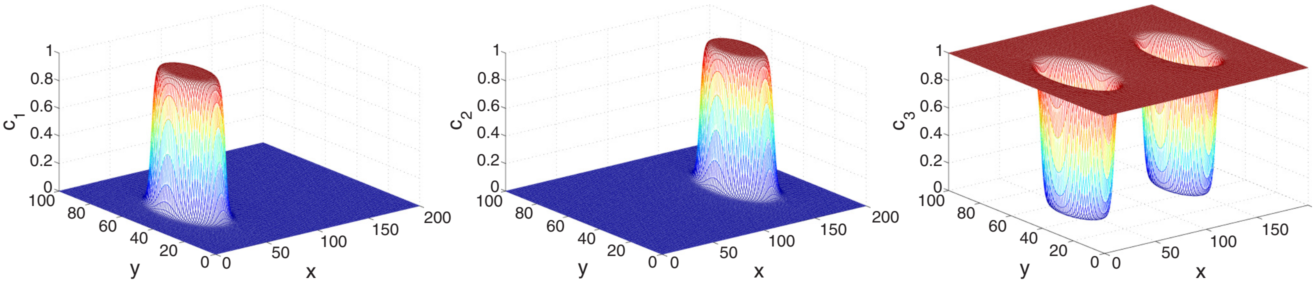

(a)

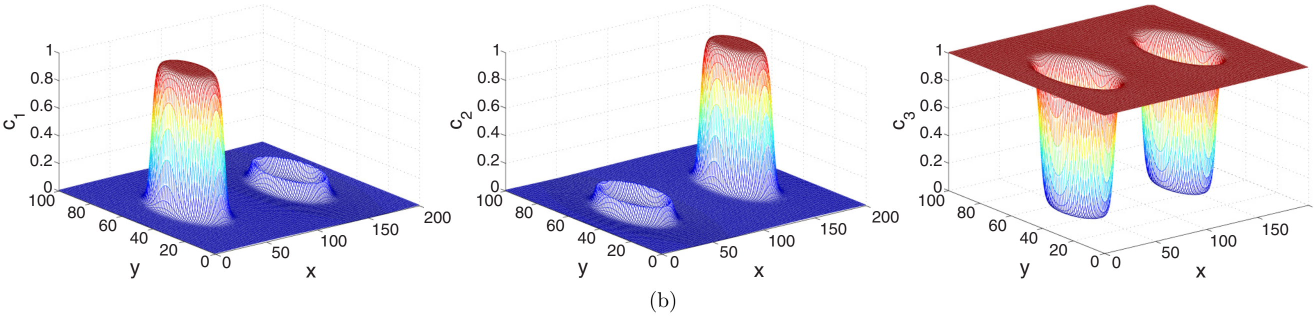

(b)

FIG. 1. The steady distributions of three order parameters (c_1, c_2, c_3) obtained by the present LB model with (a) the current bulk free energy $F = F_0$; (b) the previous bulk free energy [10,11].

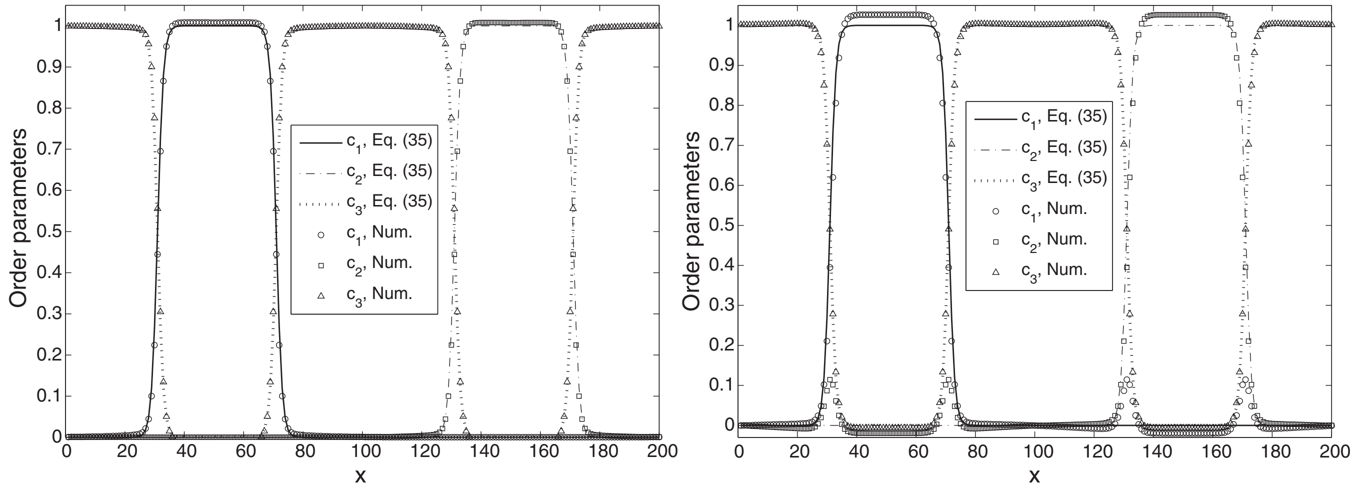

(a) (b)

FIG. 2. The steady distributions of three order parameters (c_1,c_2,c_3) along the horizontal center line ($y = N_y/2$) obtained by the present LB model with (a) the current bulk free energy $F = F_0$; (b) the previous bulk free energy [10,11].

can clearly observe that the order profiles obtained by the LB simulations with the current bulk free energy match the initial solutions closely. In contrast, some obvious deviations between the results of the LB simulation with the previous nonconsistent bulk free energy and the initial solutions can be seen clearly, as shown in Fig. 2(b). This discrepancy may trigger numerical instability in some cases, and the simulations blow up in a short time.

To test the convergence rate of the present model, the relative error $E_c = \sum_{x,y} \frac{|c_1(x,y)-c_1^{(0)}(x,y)|}{|c_1^{(0)}(x,y)|}$ is used, where $c_1^{(0)}(x,y)$ is the initial solution of the phase field c_1. We computed the relative errors with different lattice sizes and show the results in Fig. 3. As seen from the figure, the present model with the consistent bulk free energy $F = F_0$ has a nearly second-order convergence rate in space, while the model with the previous bulk free energy [10,11] has only a first-order accuracy. In addition, it is also observed that the magnitudes of the relative error of the consistent model are smaller than those of the nonconsistent model.

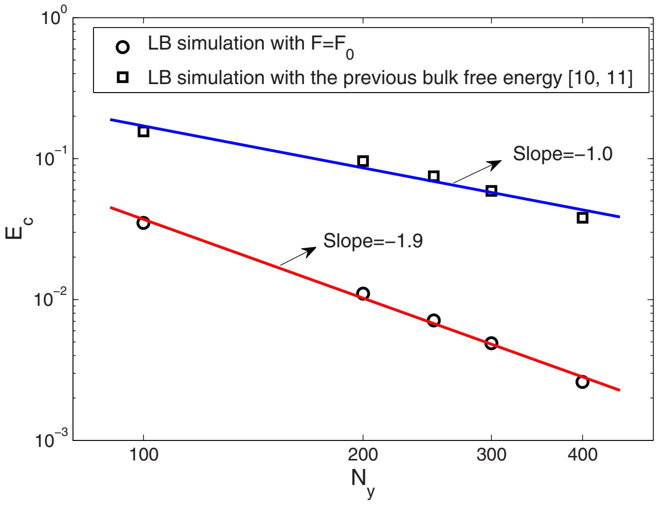

FIG. 3. The relative errors of order parameter c_1 at different lattice sizes. The solid lines represent the results of the linear fitting.

B. Ternary spinodal decomposition

Spinodal decomposition, also called phase or component separation, is an important property of mixture fluids. When a homogeneous mixture in a metastable state is imposed by some tiny concentration fluctuations, the fluid system is unstable and spinodal decomposition will take place. To the best of our knowledge, most of the previous numerical studies on this problem are confined to the two-phase situation [24,35,57,58], and relatively little attention has been paid to the three-phase case [13,59]. In this subsection, the ternary spinodal decomposition is simulated using the present model with the consistent bulk free energy $F = F_0$. This exercise is devoted to the demonstration of the capability of the present model in the study of three-component separation. The computational mesh used is 200 × 200 with periodic boundary conditions at all boundaries, and the initial profiles of the order parameters are given as

$$\begin{aligned} c_1(x,y) &= \tfrac{1}{3} + \texttt{rand}(x,y),\\ c_2(x,y) &= \tfrac{1}{3} + \texttt{rand}(x,y), \end{aligned} \tag{36}$$

where $\texttt{rand}(x,y)$ is a random function with the maximum amplitude of 0.01 and is used to impose a small random perturbation on the density field. Some physical parameters in our simulation are fixed as $\sigma_{12} = \sigma_{13} = \sigma_{23} = 0.01$, $M_0 = 0.003$, $\rho_1 = 1$, $\rho_2 = 5$, $\rho_3 = 10$, $\tau_g = 0.8$, and the rest are the same as those in the last test. Figure 4 shows the time evolution of the density distribution during the separating process. It can be clearly observed from Fig. 4 that the small perturbation is enlarged and some small drops emerged at the early stage. The small drops increase in size, and some of them may merge into larger ones as time goes on. Finally, the component represented by c_3 is totally separated from the other two components. The present numerical results are qualitatively consistent with some previous studies [13,59].

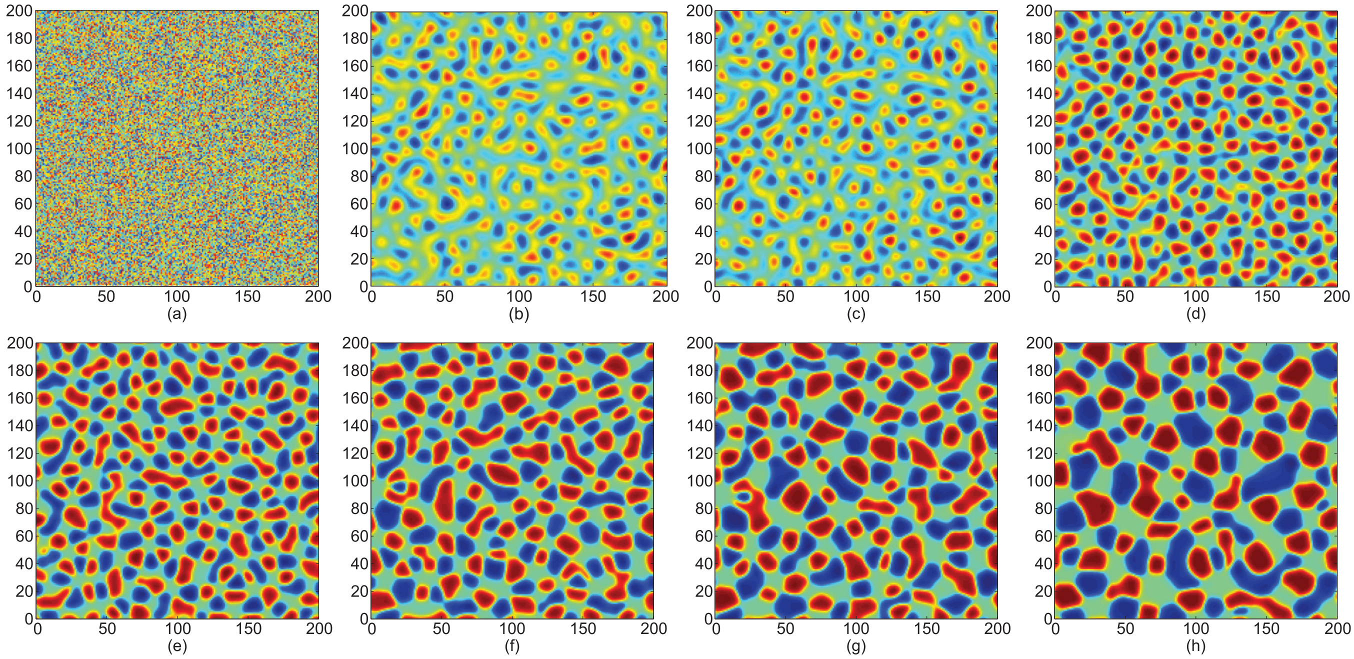

(a) (b) (c) (d) (e) (f) (g) (h)

FIG. 4. Time evolution of the density distribution during the separating process: (a) $t = 0$; (b) $t = 10\,000$; (c) $t = 20\,000$; (d) $t = 25\,000$; (e) $t = 30\,000$; (f) $t = 35\,000$; (g) $t = 40\,000$; (h) $t = 50\,000$.

C. Spreading of a liquid lens

The spreading of a liquid lens is a very classic benchmark problem and has been widely used in the literature [5,12,13,42] to test the numerical approaches for three-phase flows. In this subsection, the spreading of a liquid lens was simulated to validate the present LB model. As we know, if a circular lens is initially located at the interface between the other two immiscible fluids, it will undergo the deformation under the influence of the surface tensions until reaching its equilibrium state. According to Neumann's law [60], the equilibrium shape of the lens is determined by the three surface tension coefficients,

$$\cos(\theta_1) = \frac{\sigma_{23}^2 + \sigma_{12}^2 - \sigma_{13}^2}{2\sigma_{23}\sigma_{12}}, \quad \cos(\theta_2) = \frac{\sigma_{23}^2 + \sigma_{13}^2 - \sigma_{12}^2}{2\sigma_{23}\sigma_{13}}, \tag{37}$$

where θ_i $(i = 1,2)$ is the contact angle as illustrated in Fig. 5. The theoretical length (d) between triple junctions at the equilibrium state can be presented as [60]

$$\left(\frac{d}{2}\right)^2 \sum_{j=1}^{2} \frac{1}{\sin(\theta_j)}\left[\frac{\theta_j}{\sin(\theta_j)} - \cos(\theta_j)\right] = A, \tag{38}$$

where A is the lens area. With simple geometrical manipulations, the relation between the height $(h_1,\ h_2)$ and the length (d) can be given by

$$h_j = \frac{1 - \cos(\theta_j)}{\sin(\theta_j)}\left(\frac{d}{2}\right), \quad j = 1,2. \tag{39}$$

In this test, the computational grid is first adopted as $N_x \times N_y = 150 \times 150$. The boundary conditions are set to be periodic in x direction, and the upper and lower boundaries are the solid wall imposed by the no-slip bounce back boundary condition. The profiles of the order parameters are initialized by

$$c_1(x,y) = 0.5 + 0.5\tanh\left[2\frac{R - (x - x_c)^2 + (y - y_c)^2}{D}\right],$$
$$c_2(x,y) = \max\left[0.5 + 0.5\tanh\frac{2(y - y_c)}{D} - c_1(x,y),\ 0\right], \tag{40}$$

where R is the radius of the circular lens with a value of 30, and (x_c, y_c) is the coordinate of the lens center. The other physical parameters in our simulations are fixed as $\rho_1 = 10$, $\rho_2 = 1$, $\rho_3 = 5$, $M_0 = 0.01$, $D = 4.0$, $\tau_1 = \tau_2 = \tau_g = 0.8$. Figure 6 shows the equilibrium shapes of the lens at three

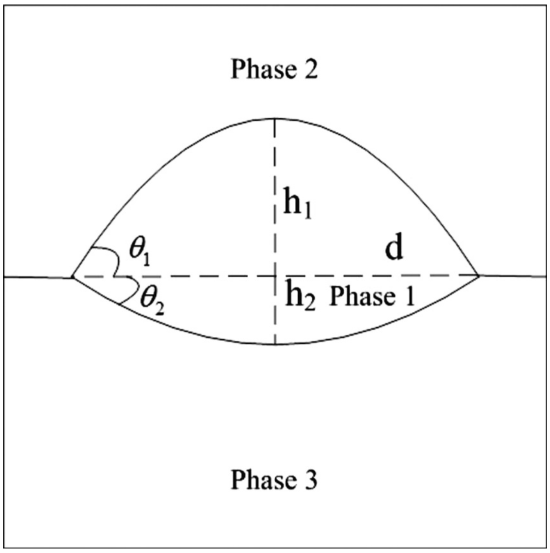

FIG. 5. Schematic of the lens shape at the equilibrium state.

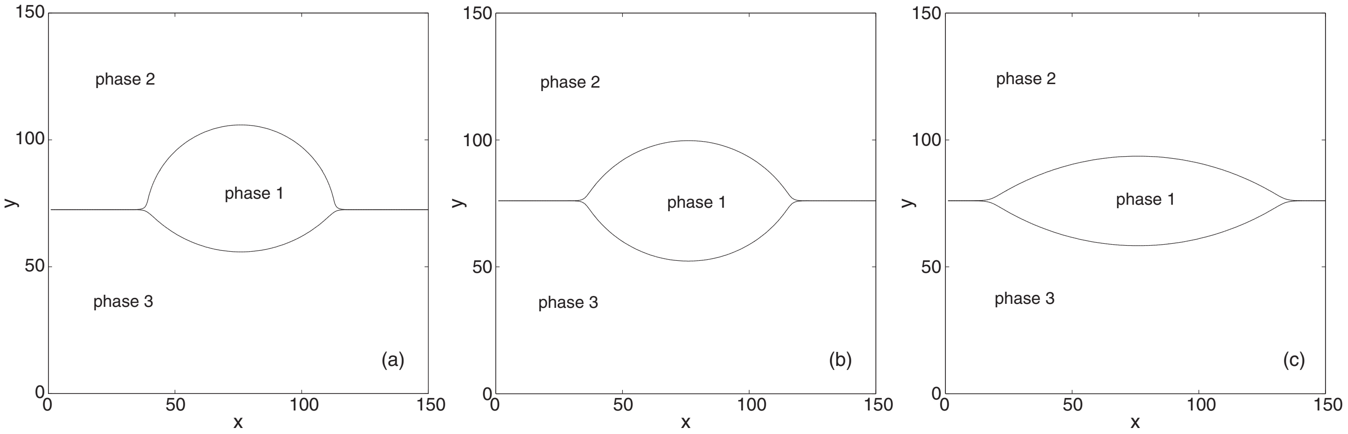

FIG. 6. The equilibrium shapes of the lens at different surface tension ratios: (a) $\sigma_{12}{:}\sigma_{13}{:}\sigma_{23} = 1{:}\frac{4}{3}{:}1$; (b) $\sigma_{12}{:}\sigma_{13}{:}\sigma_{23} = 1{:}1{:}1$; (c) $\sigma_{12}{:}\sigma_{13}{:}\sigma_{23} = 0.6{:}0.6{:}1$.

typical surface tension ratios ($\sigma_{12}{:}\sigma_{13}{:}\sigma_{23} = 1{:}\frac{4}{3}{:}1$, 1:1:1, and 0.6:0.6:1). Since the conditions $\lambda_i > 0$ and $\lambda_i > \frac{\lambda_T}{2}$ can be satisfied, the bulk free energy F_0 is algebraically and dynamically consistent and is adopted in these simulations. From Fig. 6, we can see that the lens will undergo some deformations due to the surface tension effect and eventually forms into distinct interface shapes at different surface tension coefficients. The shapes of the liquid interface in the current study compare well with the previous results [5,12]. To give a quantitative comparison, we also measured the contact angles θ_1 and θ_2 and present the results in Table I together with the analytical solutions. Here from simple geometry, the numerical contact angles θ_1 and θ_2 are obtained based on the following relations:

$$\tan\left(\frac{\theta_1}{2}\right) = \frac{2h_1}{d}, \quad \tan\left(\frac{\theta_2}{2}\right) = \frac{2h_2}{d}, \tag{41}$$

where h_1, h_2 are the measured heights, and d is the measured length. It is clearly observed from Table I that the numerical predictions of the contact angles θ_1 and θ_2 are in agreement with the corresponding theoretical values. The relative error for the θ_1 is smaller than 0.9%, while the relative error of θ_2 is less than 5.0%. We further compare the length (d) between triple junctions and the height (h_1, h_2) calculated by the present model with the corresponding theoretical values and summarize the results in Table II. It is seen that the comparison between our numerical results and the analytical solutions shows good agreement in general. The maximum relative error of the lens length (d) is about 3.1%, while the maximum relative errors for both the heights h_1 and h_2 are smaller than 2.4% and 7.7%, respectively. Here we also display the spurious velocities generated by the present model. It is shown that the maximum magnitude of the spurious velocities has an order of 10^{-5}, which is enough small so that they almost have no effect on the simulated results.

As mentioned above, if the condition $\lambda_i > \frac{\lambda_T}{2}$ is not satisfied, the model with the bulk free energy F_0 could not be dynamically consistent, which may induce some unphysical phenomena. For this reason, a more advanced bulk free energy [Eq. (10)] with the nonzero λ is a better choice and can be used to overcome above shortcoming. To illustrate this point, a comparison between them was conducted with this example. In these simulations, the computational grid is set to be 200 × 200, and the surface tension ratio is fixed as $\sigma_{12}{:}\sigma_{13}{:}\sigma_{23} = 0.5{:}0.55{:}1$ such that the condition $\lambda_1 > \frac{\lambda_T}{2}$ is not ensured. Figure 7 depicts the steady shapes of the lens obtained by the LB model with both the bulk free energy F_0 and the bulk free energy [Eq. (10)] with $\lambda = 0.1$. It is seen that the interface shows similar behavior. The computed contact angles θ_1 and θ_2 for both cases are 19.3° and 17.8°, which match the analytical ones ($\theta_1 = 18.6°$ and $\theta_2 = 16.9°$) closely. To show the effect of the bulk free energy, however, we plotted quantitatively the distributions of the order parameter c_1 in Fig. 8. It can be observed that there exists some unphysical apparitions in the results of the model with $F = F_0$, while the model with Eq. (10) can eliminate these unphysical apparitions. Furthermore, we also present the c_1 distribution at the line $x = 12$ in Fig. 9, where the LB models with $F = F_0$ produce a larger error than those of the model with Eq. (10). Therefore the bulk free energy Eq. (10) is a better choice in coping with the case with $\lambda_i \leqslant \frac{\lambda_T}{2}$.

TABLE I. The equilibrium contact angles θ_1 and θ_2 in the lens spreading test.

Surface tension ratios	Present LB model		Analytical solutions		Relative errors	
($\sigma_{12}{:}\sigma_{13}{:}\sigma_{23}$)	θ_1	θ_2	θ_1	θ_2	θ_1	θ_2
$1{:}\frac{4}{3}{:}1$	83.6°	50.0°	83.5°	52.5°	0.1%	5.0%
1:1:1	60.9°	60.9	60.8°	60.8°	0.2%	0.2%
0.6:0.6:1	34.3°	34.5°	34.0°	34.0°	0.9%	1.5%

TABLE II. The equilibrium length (d) and height (h_1, h_2) in the lens spreading test.

Surface tension ratios	Present LB model			Analytical solutions			Relative errors		
(σ_{12}:σ_{13}:σ_{23})	d	h_1	h_2	d	h_1	h_2	d	h_1	h_2
1:$\frac{4}{3}$:1	75.5	33.7	16.9	73.8	32.9	18.2	2.3%	2.4%	7.7%
1:1:1	83.1	24.0	24.0	80.7	23.7	23.7	2.9%	1.3%	1.3%
0.6:0.6:1	117.5	17.7	17.7	113.9	17.4	17.4	3.1%	1.7%	1.7%

We now consider the effect of the gravity on the equilibrium configuration of the interface. According to the de Gennes theory [61], the equilibrium shape of the interface depends on the relative importance of the gravity and the surface tensions. When the surface tension dominates over the gravity, the middle phase may form into a lens. Otherwise, it may form a puddle, and the asymptotic thickness (H) of the puddle can be analytically given by [61,62]

$$H = \sqrt{\frac{2(\sigma_{12} + \sigma_{13} - \sigma_{23})}{\frac{\rho_1}{\rho_3}(\rho_3 - \rho_1)g}}. \tag{42}$$

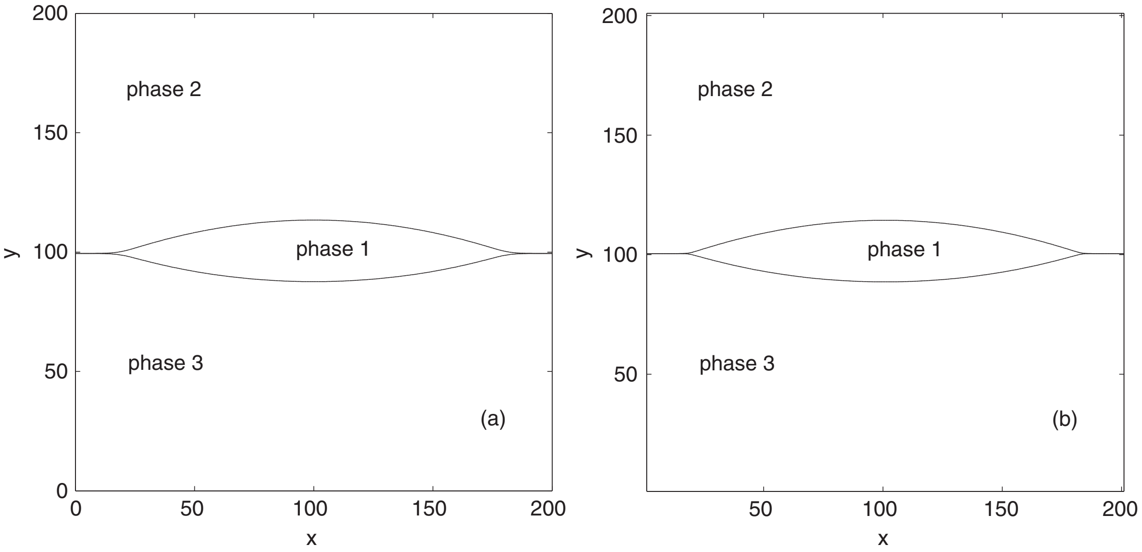

FIG. 7. The equilibrium shapes of the lens with the surface tension ratio σ_{12}:σ_{13}:σ_{23} = 0.5:0.55:1 obtained by the present LB model: (a) the bulk free energy $F = F_0$; (b) the bulk free energy [Eq. (10)] with $\lambda = 0.1$.

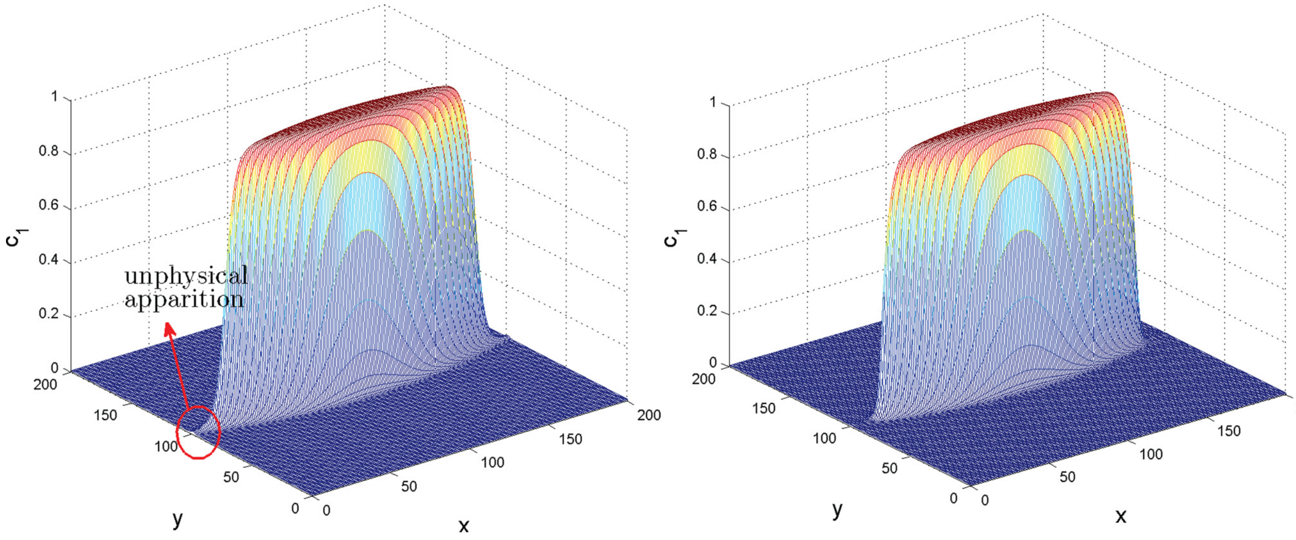

(a) (b)

FIG. 8. The steady distributions of the order parameter c_1 obtained by the present LB model with (a) the bulk free energy $F = F_0$; (b) the bulk free energy Eq. (10) with $\lambda = 0.1$.

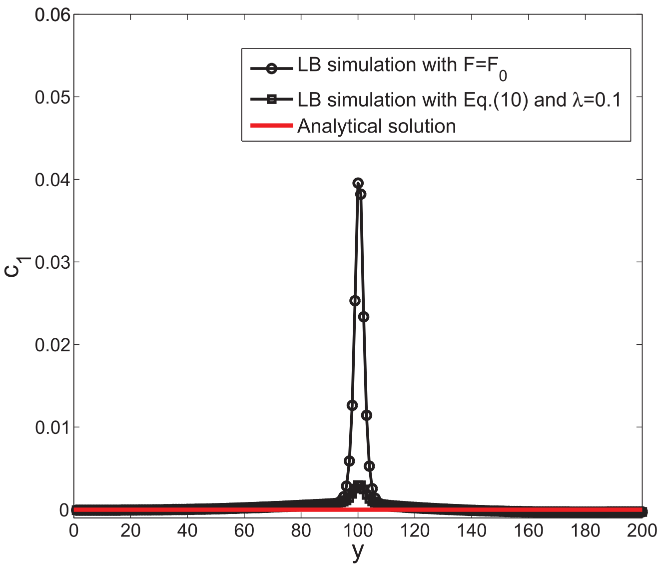

FIG. 9. The steady distributions of the order parameter c_1 along the line $x = 12$ obtained by the present LB model with (a) the bulk free energy $F = F_0$; (b) the bulk free energy Eq. (10) with $\lambda = 0.1$.

To incorporate the gravitational effect, in our simulations the body force $\mathbf{G} = (0, -\rho g)$ is imposed on the fluids, where g is the gravity acceleration. Due to the large deformation of the interface, the computational domain is increased to $N_x \times N_y = 300 \times 150$. The physical parameters are set to be $\rho_1 = 5$, $\rho_2 = 1$, $\rho_3 = 10$, and $\sigma_{12} = \sigma_{23} = 0.01$. Figure 10 shows the equilibrium shapes of the interface at three typical values of the gravitational acceleration. It can be seen from Fig. 10 that at a low gravity, the middle phase forms a lens, which is made of two circular caps. As the gravity magnitude increases, the shape of the middle phase becomes flatter. When the gravity is sufficiently large, the interface undergoes a large deformation and a puddle is formed. The present numerical results are qualitatively consistent with the de Gennes theory [61]. We further conducted a quantitative comparison of the asymptotic thickness as a function of gravity between the current simulation and the de Gennes theory and present the results in Fig. 11. It can be observed that at a large gravity, the numerical prediction agrees well with the corresponding theoretical one. While at a small gravity, an obvious deviation between them can be observed. This is because that the shape of the interface is no longer that of a puddle when the gravity is very small, and the theoretical formula (42) is invalid in this case. The similar result was also reported in the previous study [15].

The effect of surface tension on the equilibrium configuration of the interface is also examined. Here we vary the surface tension between 1-phase and 3-phase, while fixing the gravity acceleration at $g = 1 \times 10^{-5}$. Figure 12 depicts the equilibrium shapes of the interface at two typical values of σ_{13}. It can be seen that the interface shows a larger deformation and becomes flatter at a smaller surface tension. To quantitatively show the surface tension effect, we plot the asymptotic thickness in Fig. 13. For a comparison, the results of the de Gennes theory [61] are also presented. From Fig. 13, we can see that the asymptotic thickness increases with the surface tension σ_{13}. In addition, the comparison between

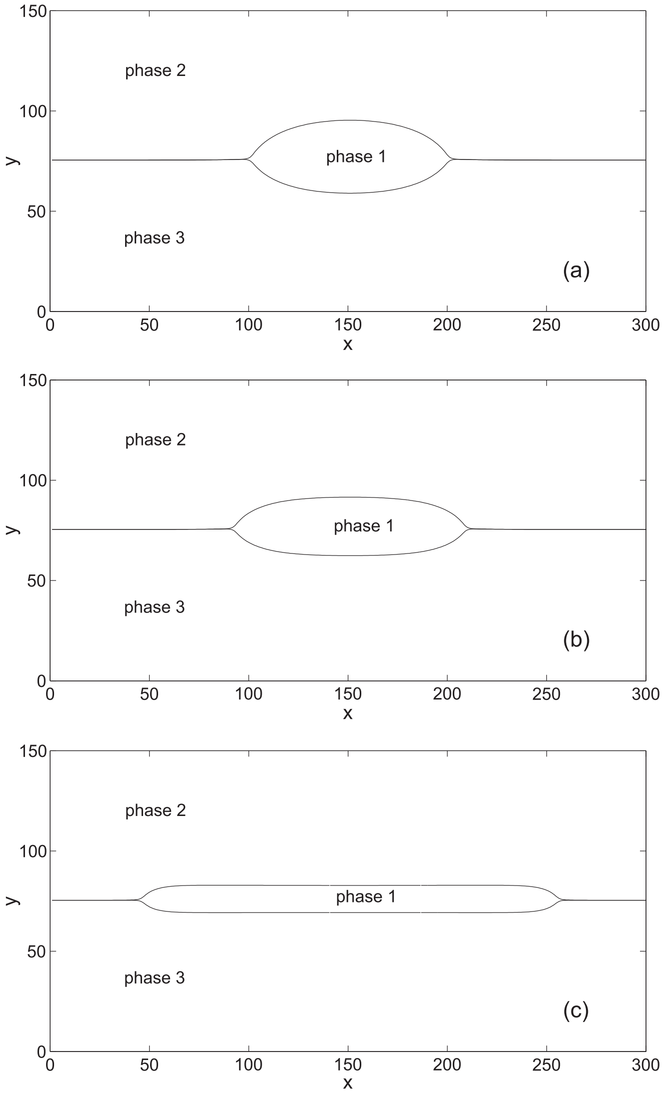

FIG. 10. The equilibrium shapes of the interface at different gravity forces: (a) $g = 5 \times 10^{-6}$; (b) $g = 1 \times 10^{-5}$; (c) $g = 5 \times 10^{-5}$. The surface tension σ_{13} is fixed to be 0.01.

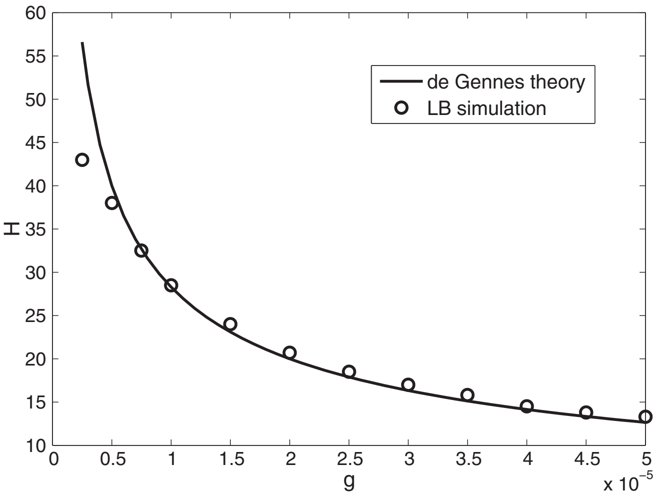

FIG. 11. Comparison of the asymptotic thickness as a function of gravity between the current simulation and the de Gennes theory [61]. The surface tension σ_{13} is fixed to be 0.01.

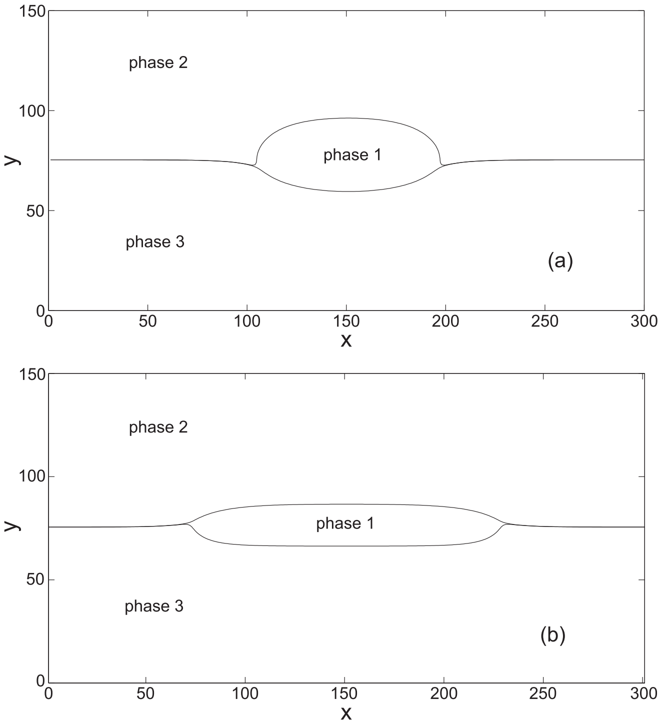

FIG. 12. The equilibrium shapes of the interface at different surface tensions: (a) $\sigma_{13} = 0.018$; (b) $\sigma_{13} = 0.004$. The gravity acceleration is 1×10^{-5}.

the simulated results and the theoretical values shows good agreement in general.

D. Kelvin-Helmholtz instability

To show the capacity of the present model in dealing with complex fluid systems, here we also consider the Kelvin-Helmholtz instability (KHI) with a more complicated interfacial dynamics. KHI is a fundamental interfacial instability in fluid mechanics, which occurs when a small perturbed interface between fluids is subject to a parallel shear flow [63]. The study of this instability is extremely important since it plays a dominant role in the understanding of turbulent mixing processes [64,65]. Due to its important applications, the KHI has been widely investigated by using analytical [66,67], experimental [68], as well as numerical [33,69–72] approaches. However, most of the previous works dealt with the KHI at the interface of a two-phase system [33,67–71] and the numerical studies on the KHI of three-component systems are quite limited due to the complexity of interfacial dynamics and the rareness of a robust numerical approach. To fill this gap, we will apply the present LB model to simulate the immiscible KHI of three-component fluids.

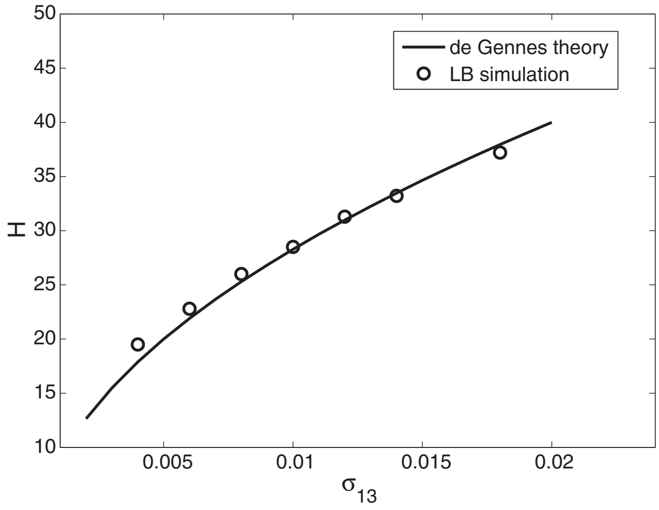

FIG. 13. Comparison of the asymptotic thickness as a function of surface tension between the current simulation and the de Gennes theory [61]. The gravity acceleration is 1×10^{-5}.

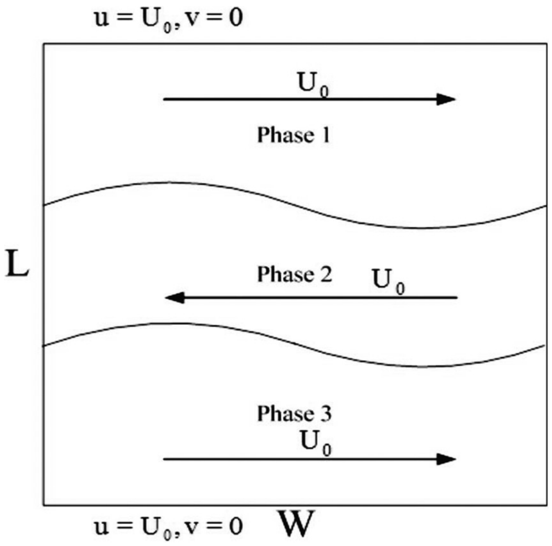

FIG. 14. Schematic of the initial setup in the three-component immiscible KHI test.

The physical problem we considered here is a square box with an aspect ratio of $L \times W$, where L and W are the box length and width. As illustrated in Fig. 14, the initial interfaces are located at $y_1 = \frac{L}{3}$ and $y_2 = \frac{2L}{3}$, with an imposed sinusoidal perturbation:

$$h = 0.01L \sin\left(\frac{4\pi x}{W}\right). \tag{43}$$

To be smoothed across the interface, the initial profiles of the order parameters are given by

$$\begin{aligned} c_1(x,y) &= 0.5 + 0.5 \tanh 2\left(\frac{y - y_2 - h}{D}\right), \\ c_2(x,y) &= 0.5 + 0.5 \tanh 2\left(\frac{y - y_1 - h}{D}\right) - c_1(x,y), \end{aligned} \tag{44}$$

and similar to Ref. [72], we seed the initial distribution for fluid velocity (u,v) as

$$\begin{aligned} u &= U_0 + U_0\left[\tanh 2\left(\frac{y - y_2 - h}{D}\right) - \tanh 2\left(\frac{y - y_1 - h}{D}\right)\right], \\ v &= 0, \end{aligned} \tag{45}$$

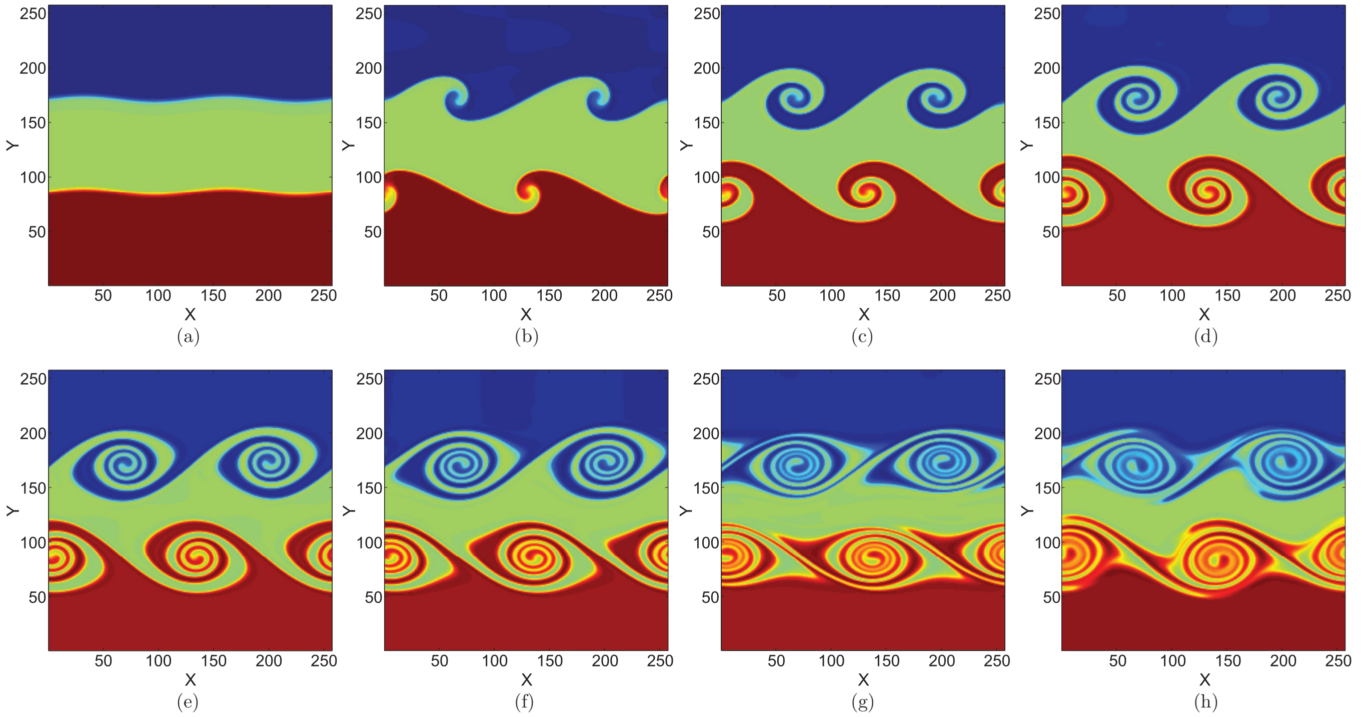

(a) (b) (c) (d) (e) (f) (g) (h)

FIG. 15. Evolution of the density contours in the immiscible KHI of three-component fluids: (a) $t = 0$; (b) $t = 2000$; (c) $t = 3000$; (d) $t = 4000$; (e) $t = 5000$; (f) $t = 6000$; (g) $t = 7500$; (h) $t = 9000$.

where U_0 is half the velocity difference across the shear layer. The dimensionless Reynolds number characterizing the KHI is defined as

$$\mathrm{Re} = \frac{LU_0}{\nu}. \tag{46}$$

The simulation was carried out in a $L \times W = 256 \times 256$ lattice with the periodic boundary condition in the horizontal direction. The velocities for the upper and lower plates are fixed at $u = U_0$ and $v = 0$, and the nonequilibrium extrapolation scheme [73] is utilized to treat these boundaries. The remaining physical parameters in our simulation are set as $\mathrm{Re} = 5000$, $\rho_1:\rho_2:\rho_3 = 0.98:0.99:1$, $\sigma_{12} = \sigma_{13} = \sigma_{23} = 1 \times 10^{-4}$, $U_0 = 0.04$, $M_0 = 2 \times 10^{-4}$, $D = 4$, $\tau_1 = \tau_2 = 0.8$. Since the condition $\lambda_i > \frac{\lambda_T}{2}$ can be satisfied, the simple bulk free energy F_0 is adopted in this simulation. Figure 15 depicts the evolution of the density contours in the immiscible KHI of three-component fluids. It can be observed, due to the shear effect, the middle fluid penetrates into the upper and lower ones at early time, while the interfaces among them gradually roll up. As time goes on, several pair of vortices then appear and the flow region becomes nonlinear, which leads to the formation of the main billows. These vortices continue to grow in size, and the structure becomes more and more complex at late time. The above behaviors of the liquid interfaces obtained by the present model are in line with the previous results presented in Fig. 8 of Ref. [72]. We also calculated the vorticity magnitudes $(\partial_x v - \partial_y u)$ in the KHI and presented the results in Fig. 16. It is found that the vorticity gradually accumulates in the billow region, and the strength becomes larger as time advances. As a result, a large vorticity concentrates in the cores of the vortex pairs. The vortices develop further and become chaotic at late time, which leads to the formation of several secondary vortices at the vicinity of fluid interfaces. It is also observed from Fig. 16 that the vortex structures match the corresponding density patterns closely at the early stage, while they become more complex than the density patterns at the late stage.

V. SUMMARY

In this paper, a LB model based on the multicomponent phase-field theory is proposed for three-phase flow systems. This model utilizes three LB evolution equations, two of which are used for capturing the interfaces among three-phase fluids and the third is adopted to to solve flow fields. The distribution function for the force term is modified in the LB equation for flow field, which seems more reasonable from the multiscale analysis, and simultaneously, the calculation of the velocity can be much simpler. The multiscale analysis also demonstrates that both the multicomponent CH equations and the NS equations can be recovered correctly from the present model. In addition, due to the particular choice of bulk free energy, the present model is well posed and also shows algebraical and dynamical consistency properties with the binary one. To test the performance of the present model, a series of numerical experiments, including two circular interfaces, the ternary spinodal decomposition, the spreading of a liquid lens, and the Kelvin-Helmholtz instability, have been conducted. It is found that the present model with the consistent bulk free energy is able to capture the interface more accurately than the one with the previous bulk free energy. Furthermore, it is also shown that the numerical results of three-phase flows agree well with the the analytical solutions or available data, which demonstrates that the present LB model is a reliable and efficient method for studying three-phase flow problems.

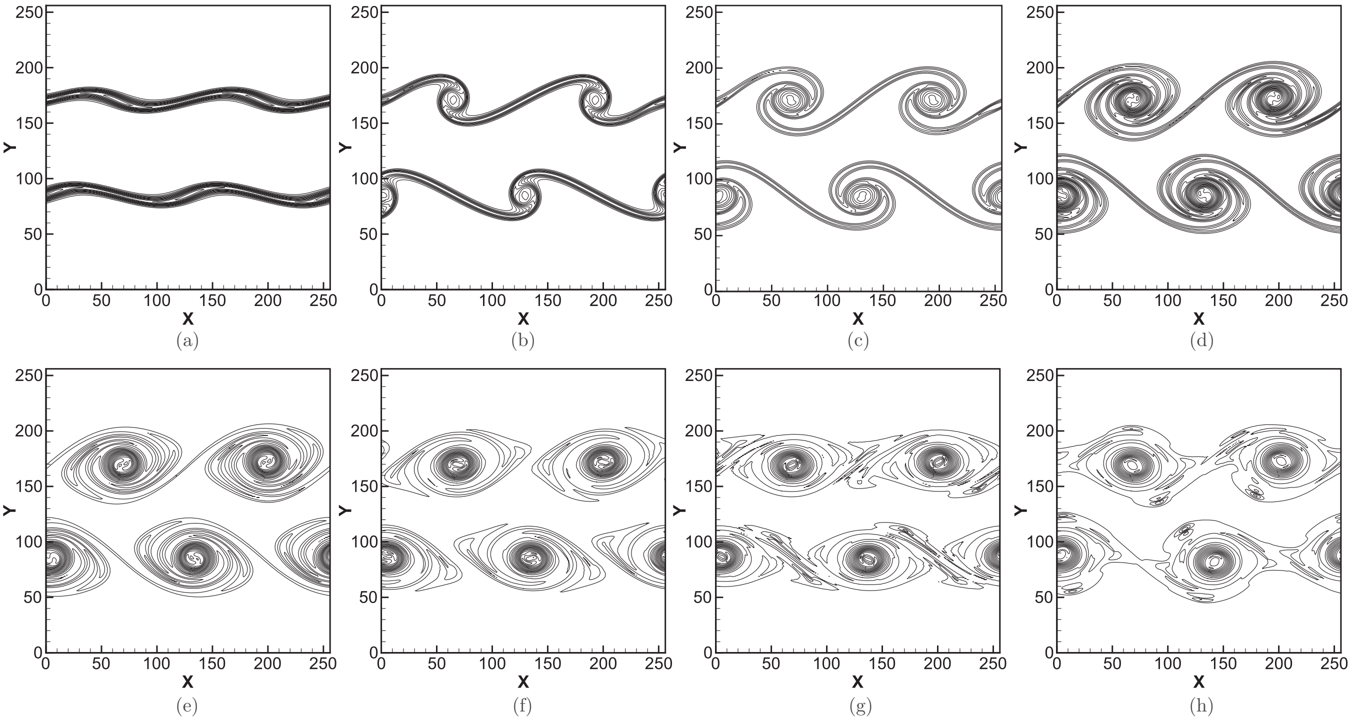

(a) (b) (c) (d)

(e) (f) (g) (h)

FIG. 16. Evolution of the vorticity magnitudes in the immiscible KHI of three-component fluids: (a) $t = 0$; (b) $t = 2000$; (c) $t = 3000$; (d) $t = 4000$; (e) $t = 5000$; (f) $t = 6000$; (g) $t = 7500$; (h) $t = 9000$.

Finally, we give a discussion on the maximum density ratio among three fluid components that can be reached by our model. It is shown that the critical density ratio depends on the flow velocity. In the test of the lens spreading where the fluid velocity is very small, our model can deal with the case with the density ratio of about 100. We also simulated a dynamic case of the ternary spinodal decomposition with the present model. It is found that our model is stable at the largest density ratio of about 20. To our best knowledge, to develop a large-density-ratio model is still an attractive problem in the framework of the LB method. It may benefit from the extra flexibility to overcome the limitation on the density ratio if some approaches are adopted, such as introducing a nonuniform mobility in the Cahn-Hilliard equation, using a more stable difference scheme [32], or adopting a flux solver LB method [74]. The present scheme is developed based on the BGK collision operator for its simplicity and high computational efficiency. The construction can be easily generalized to the case with a more advanced multiple-relaxation-time collision model [75]. And also, the extension to the three-dimensional case can be conducted directly. These will be considered in our future works.

ACKNOWLEDGMENTS

This work is financially supported by the National Natural Science Foundation of China (Grants No. 11272132, No. 51576079, and No. 51306133) and the Natural Science Foundation of Hubei Province (Grant No. 2015CFB440).

APPENDIX: CHAPMAN-ENSKOG ANALYSIS OF THE PRESENT LB MODEL FOR THE NAVIER-STOKES EQUATIONS

We now conduct the CE analysis to show the consistency of the LB evolution equation (22) to the NS equations (14). From Eqs. (23) and (25), one can derive the following moment conditions:

$$\begin{gathered}\sum_k g_k^{eq} = 0, \sum_k e_{k\alpha} g_k^{eq} = \rho u_\alpha,\\ \sum_k e_{k\alpha} e_{k\beta} g_k^{eq} = \rho u_\alpha u_\beta + p\delta_{\alpha\beta}, \sum_k e_{k\alpha} e_{k\beta} e_{k\gamma} g_k^{eq} = \rho c_s^2 \Delta_{\alpha\beta\gamma\theta} u_\theta,\end{gathered} \tag{A1}$$

$$\begin{aligned}\sum_k G_k = \left(1 - \frac{1}{2\tau_g}\right) u_\alpha \partial_\alpha \rho, \sum_k e_{k\alpha} G_k = \left(1 - \frac{1}{2\tau_g}\right) F_\alpha + F_{a\alpha}, \Lambda =: \sum_k e_{k\alpha} e_{k\beta} G_k\\ = \left(1 - \frac{1}{2\tau_g}\right)[u_\alpha F_\beta + u_\beta F_\alpha + u_\alpha \partial_\beta (\rho c_s^2) + u_\beta \partial_\alpha (\rho c_s^2) + (u_\gamma \partial_\gamma \rho c_s^2)\delta_{\alpha\beta}],\end{aligned} \tag{A2}$$

where $\Delta_{\alpha\beta\gamma\theta} = \delta_{\alpha\beta}\delta_{\gamma\theta} + \delta_{\alpha\gamma}\delta_{\beta\theta} + \delta_{\alpha\theta}\delta_{\beta\gamma}$, and the terms of $O(\mathrm{Ma}^3)$ have been omitted from Eq. A(2) in the incompressible limit. To derive the macroscopic equations, we first introduce the following multiscale expansions:

$$g_k = g_k^{(0)} + \epsilon g_k^{(1)} + \epsilon^2 g_k^{(2)} + \cdots, \tag{A3a}$$

$$\partial_t = \epsilon\partial_{t_1} + \epsilon^2\partial_{t_2}, \partial_\alpha = \epsilon\partial_{1\alpha}, \tag{A3b}$$

$$G_k = \epsilon G_k^{(1)} + \epsilon^2 G_k^{(2)}, F_\alpha = \epsilon F_\alpha^{(1)}, F_{a\alpha} = \epsilon^2 F_{a\alpha}^{(2)}. \tag{A3c}$$

Applying the Taylor expansion and the above formulas, Eq. (22) can be expanded into a series of equations in different order of ϵ,

$$\epsilon^0 : g_k^{(0)} = g_k^{(eq)}, \tag{A4a}$$

$$\epsilon^1 : D_{1k} g_k^{(0)} = -\frac{1}{\tau_g \delta_t} g_k^{(1)} + G_k^{(1)}, \tag{A4b}$$

$$\epsilon^2 : \partial_{t_2} g_k^{(0)} + D_{1k} g_k^{(1)} + \frac{\delta_t}{2} D_{1k}^2 g_k^{(0)} = -\frac{1}{\tau_g \delta_t} g_k^{(2)} + G_k^{(2)}, \tag{A4c}$$

where $D_{1k} = \partial_{t_1} + e_{k\alpha}\partial_{1\alpha}$. With the help of Eq. (A4b), Eq. (A4c) can be further simplified as

$$\partial_{t_2} g_k^{(0)} + D_{1k}\left(1 - \frac{1}{2\tau_g}\right) g_k^{(1)} = -\frac{1}{\tau_g \delta_t} g_k^{(2)} - \frac{\delta_t}{2} D_{1k} G_k^{(1)} + G_k^{(2)}. \tag{A5}$$

Based on Eqs. (A1) and (A2), the zero-order moment of g_k can be defined by [37]

$$\sum_k g_k = -\frac{\delta_t}{2} u_\alpha \partial_\alpha \rho. \tag{A6}$$

Applying the multiscaling expansions to Eqs. (28) and (A6), and using Eqs. (A1) and (A2), one can easily derive

$$\sum_k g_k^{(1)} = -\frac{\delta_t}{2} u_\alpha \partial_{1\alpha}\rho, \quad \sum_k g_k^{(n)} = 0, (n \geqslant 2), \tag{A7}$$

$$\sum_k e_{k\alpha} g_k^{(1)} = -\frac{\delta_t}{2} F_\alpha^{(1)}, \quad \sum_k e_{k\alpha} g_k^{(n)} = 0, (n \geqslant 2). \tag{A8}$$

Summing Eq. (A4b), and Eq. (A4b) multiplied by $e_{k\beta}$ over k, respectively, the recovered equations at ϵ scale can be obtained,

$$\partial_{1\alpha} u_\alpha = 0, \tag{A9}$$

$$\partial_{t_1}(\rho u_\beta) + \partial_{1\alpha}(\rho u_\alpha u_\beta + p\delta_{\alpha\beta}) = F_\beta^{(1)}, \tag{A10}$$

where Eqs. (A1), (A2), (A7), and (A8) have been utilized.

In a similar way, from Eq. (A5) one can obtain the recovered equations at ϵ^2 scale,

$$\partial_{t_1}\left(-\frac{\delta_t}{2} u_\alpha \partial_{1\alpha}\rho\right) + \partial_{1\alpha}\left(-\frac{\delta_t}{2} F_\alpha^{(1)}\right) = -\frac{\delta_t}{2}\left[\partial_{t_1}(u_\alpha \partial_{1\alpha}\rho) + \partial_{1\alpha} F_\alpha^{(1)}\right], \tag{A11}$$

$$\partial_{t_2}(\rho u_\beta) + \left(1 - \frac{1}{2\tau_g}\right)\partial_{1\alpha}\Pi^{(1)} = -\frac{\delta_t}{2}\partial_{1\alpha}\Lambda^{(1)} + F_{a\beta}^{(2)}, \tag{A12}$$

where $\Pi^{(1)} = \sum_k e_{k\alpha} e_{k\beta} g_k^{(1)}$ is the first-order momentum flux tensor, and $\Lambda = \epsilon\Lambda^{(1)}$. From Eq. (A4b), we can get

$$\begin{aligned}\Pi^{(1)} &= \sum_k e_{k\alpha} e_{k\beta} g_k^{(1)} = -\tau_g \delta_t \sum_k e_{k\alpha} e_{k\beta}\left[D_{1k} g_k^{(0)} - G_k^{(1)}\right] \\ &= -\tau_g \delta_t c_s^2[\partial_{1\alpha}(\rho u_\beta) + \partial_{1\beta}(\rho u_\alpha) + (\partial_{1\gamma}\rho u_\gamma)\delta_{\alpha\beta}] \\ &\quad + \tau_g \delta_t \Lambda^{(1)},\end{aligned} \tag{A13}$$

in which the terms of $O(\delta_t Ma^2)$ have been neglected for incompressible flows. Then the substitution of Eq. (A13) into Eq. (A12) yields

$$\partial_{t_2}(\rho u_\beta) - \partial_{1\alpha}\left\{\left(\tau_g - \frac{1}{2}\right)\delta_t c_s^2[\partial_{1\alpha}(\rho u_\beta) + \partial_{1\beta}(\rho u_\alpha) + (u_\gamma \partial_{1\gamma}\rho)\delta_{\alpha\beta}] - \tau_g \delta_t \Lambda^{(1)}\right\} = F_{a\beta}^{(2)}. \tag{A14}$$

Combining Eqs. (A9) and (A11) at ϵ and ϵ^2 scales, together with Eqs. (A10) and (A14), we have

$$\partial_\alpha u_\alpha = 0, \tag{A15}$$

$$\begin{aligned}\partial_t(\rho u_\beta) + \partial_\alpha(\rho u_\alpha u_\beta + p\delta_{\alpha\beta}) &= \partial_\alpha\{\nu[\partial_\alpha(\rho u_\beta) + \partial_\beta(\rho u_\alpha) + (u_\gamma \partial_\gamma \rho)\delta_{\alpha\beta}] - \tau_g \delta_t \Lambda\} \\ &\quad + F_\beta + F_{a\beta},\end{aligned} \tag{A16}$$

where $\nu = c_s^2 \delta_t(\tau_g - \frac{1}{2})$ is the kinematic viscosity. Multiplying ϵ on both sides of Eq. (A10), we can get

$$F_\beta = O(\mathrm{Ma}) \tag{A17}$$

for incompressible flows. Substituting Eq. (A2) into Eq. (A16) and using Eq. (A17), Eq. (A16) can be reduced to

$$\partial_t(\rho u_\beta) + \partial_\alpha(\rho u_\alpha u_\beta + p\delta_{\alpha\beta}) = \partial_\alpha \rho\nu(\partial_\alpha u_\beta + \partial_\beta u_\alpha) + F_\beta + F_{a\beta} \tag{A18}$$

with the order of $O(\delta_t \mathrm{Ma}^2)$. Furthermore, based on the identical relations

$$\partial_t(\rho u_\beta) + \partial_\alpha(\rho u_\alpha u_\beta) = \rho(\partial_t u_\beta + u_\alpha \partial_\alpha u_\beta) + u_\beta(\partial_t \rho + \partial_\alpha \rho u_\alpha) \tag{A19}$$

and

$$u_\beta(\partial_t \rho + \partial_\alpha \rho u_\alpha) = \sum_{i=1}^{3} \frac{\partial\rho}{\partial c_i}(\partial_t c_i + \partial_\alpha c_i u_\alpha) = F_{a\beta}, \tag{A20}$$

Eq. (A18) can be rewritten as

$$\rho(\partial_t u_\beta + u_\alpha \partial_\alpha u_\beta) = -\partial_\beta p + \partial_\alpha[\rho\nu(\partial_\alpha u_\beta + \partial_\beta u_\alpha)] + F_{s\beta} + G_\beta. \tag{A21}$$

From Eqs. (A15) and (A21), we can clearly see that the NS equations can be exactly recovered from the present LB model.

[1] A. Maghzi, S. Mohammadi, M. H. Ghazanfari, R. Kharrat, and M. Masihi, Exp. Therm. Fluid Sci. **40**, 168 (2012).

[2] H. Li *et al.*, J. Power Sources **178**, 103 (2008).

[3] R. Seemann, M. Brinkmann, T. Pfohl, and S. Herminghaus, Rep. Prog. Phys. **75**, 016601 (2012).

[4] H. K. Zhao, T. Chan, B. Merriman, and S. Osher, J. Comput. Phys. **127**, 179 (1996).

[5] K. A. Smith, F. J. Solis, and D. L. Chopp, Interfaces Free Bound. **4**, 263 (2002).

[6] R. I. Saye and J. A. Sethian, Proc. Natl. Acad. Sci. USA **108**, 19498 (2011).

[7] M. Muradoglu and S. Tasoglu, Comput. Fluids **39**, 615 (2010).

[8] R. Bonhomme, J. Magnaudet, F. Duval, and B. Piar, J. Fluid Mech. **707**, 405 (2012).

[9] N. Tofighi and M. Yildiz, Comput. Math. Appl. **66**, 525 (2013).

[10] H. Garcke, B. Nestler, and B. Stoth, SIAM J. Appl. Math. **60**, 295 (1999).

[11] J. Kim, K. Kang, and J. Lowengrub, Commu. Math. Sci. **2**, 53 (2004).

[12] F. Boyer and C. Lapuerta, ESAIM: Math. Model. Numer. Anal. **40**, 653 (2006).

[13] J. Kim, Comput. Methods Appl. Mech. Eng. **196**, 4779 (2007).

[14] F. Boyer, C. Lapuerta, S. Minjeaud, B. Piar, and M. Quintard, Transp. Porous Media **82**, 463 (2010).

[15] S. Dong, J. Comput. Phys. **276**, 691 (2014).

[16] S. Chen and G. Doolen, Annu. Rev. Fluid Mech. **30**, 329 (1998).

[17] Z. L. Guo and C. Shu, *Lattice Boltzmann Method and Its Applications in Engineering* (World Scientific, Singapore, 2013).

[18] I. Ginzburg, Adv. Water Resour. **28**, 1171 (2005).

[19] Z. H. Chai and B. C. Shi, Appl. Math. Model. **32**, 2050 (2008).

[20] B. C. Shi and Z. L. Guo, Phys. Rev. E **79**, 016701 (2009).

[21] X. G. Yang, B. C. Shi, and Z. H. Chai, Comput. Math. Appl. **68**, 1653 (2014).

[22] J. T. Huang and W. A. Yong, J. Comput. Phys. **300**, 70 (2015).

[23] A. K. Gunstensen, D. H. Rothman, S. Zaleski, and G. Zanetti, Phys. Rev. A **43**, 4320 (1991).

[24] X. Shan and H. Chen, Phys. Rev. E **47**, 1815 (1993).

[25] X. Shan and H. Chen, Phys. Rev. E **49**, 2941 (1994).

[26] M. Sbragaglia, R. Benzi, L. Biferale, S. Succi, K. Sugiyama, and F. Toschi, Phys. Rev. E **75**, 026702 (2007).

[27] G. Falcucci, S. Ubertini, and S. Succi, Soft Matter **6**, 4357 (2010).

[28] C. E. Colosqui, G. Falcucci, S. Ubertini, and S. Succi, Soft Matter **8**, 3798 (2012).

[29] M. R. Swift, W. R. Osborn, and J. M. Yeomans, Phys. Rev. Lett. **75**, 830 (1995).

[30] M. R. Swift, E. Orlandini, W. R. Osborn, and J. M. Yeomans, Phys. Rev. E **54**, 5041 (1996).

[31] X. He, S. Chen, and R. Zhang, J. Comput. Phys. **152**, 642 (1999).

[32] T. Lee and L. Liu, J. Comput. Phys. **229**, 8045 (2010).

[33] A. Fakhari and T. Lee, Phys. Rev. E **87**, 023304 (2013).

[34] L. Zheng, S. Zheng, and Q. Zhai, Phys. Rev. E **91**, 013309 (2015).

[35] Y. Q. Zu and S. He, Phys. Rev. E **87**, 043301 (2013).

[36] H. Liang, B. C. Shi, Z. L. Guo, and Z. H. Chai, Phys. Rev. E **89**, 053320 (2014).

[37] H. Liang, Z. H. Chai, B. C. Shi, Z. L. Guo, and T. Zhang, Phys. Rev. E **90**, 063311 (2014).

[38] H. Liu and Y. Zhang, Phys. Fluids **23**, 082101 (2011).

[39] Q. X. Li, Z. H. Chai, B. C. Shi, and H. Liang, Phys. Rev. E **90**, 043015 (2014).

[40] H. Liang, Z. H. Chai, B. C. Shi, Z. L. Guo, and Q. X. Li, Int. J. Mod. Phys. C **26**, 1550074 (2015).

[41] I. Halliday, A. P. Hollis, and C. M. Care, Phys. Rev. E **76**, 026708 (2007).

[42] T. J. Spencer, I. Halliday, and C. M. Care, Phys. Rev. E **82**, 066701 (2010).

[43] S. Leclaire, M. Reggio, and J. Trepanier, J. Comput. Phys. **246**, 318 (2013).

[44] T. Reis and T. N. Phillips, J. Phys. A: Math. Theor. **40**, 4033 (2007).

[45] J. Bao and L. Schaefer, Appl. Math. Model. **37**, 1860 (2013).

[46] Z. H. Chai and T. S. Zhao, Acta Mech. Sin. **28**, 983 (2012).

[47] Q. Li, K. H. Luo, Y. J. Gao, and Y. L. He, Phys. Rev. E **85**, 026704 (2012).

[48] H. Liu, A. J. Valocchi, Y. Zhang, and Q. Kang, Phys. Rev. E **87**, 013010 (2013).

[49] D. Jacqmin, J. Comput. Phys. **155**, 96 (1999).

[50] H. Ding, P. D. M. Spelt, and C. Shu, J. Comput. Phys. **226**, 2078 (2007).

[51] J. Shen and X. F. Yang, SIAM J. Sci. Comput. **32**, 1159 (2010).

[52] Z. L. Guo, C. G. Zheng, and B. C. Shi, Phys. Rev. E **65**, 046308 (2002).

[53] B. C. Shi, B. Deng, R. Du, and X. W. Chen, Comput. Math. Appl. **55**, 1568 (2008).

[54] Z. L. Guo, C. G. Zheng, and B. C. Shi, Phys. Rev. E **83**, 036707 (2011).

[55] Q. Lou, Z. L. Guo, and B. C. Shi, Europhys. Lett. **99**, 64005 (2012).

[56] J. Kim and J. Lowengrub, Interfaces Free Bound. **7**, 435 (2005).

[57] J. Chin and P. V. Coveney, Phys. Rev. E **66**, 016303 (2002).

[58] A. G. Xu, G. Gonnella, and A. Lamura, Physica A **331**, 10 (2004).

[59] K. A. Smith, F. J. Solis, L. Tao, K. Thornton, and M. Olvera de la Cruz, Phys. Rev. Lett. **84**, 91 (2000).

[60] J. S. Rawlinson and B. Widom, *The Molecular Theory of Capillarity* (Clarendon Press, Oxford, 1982).

[61] P. G. de Gennes, F. Brochard-Wyart, and D. Quere, *Capillarity and Wetting Phenomena* (Springer, New York, 2003).

[62] I. Langmuir, J. Chem. Phys. **1**, 756 (1933).

[63] R. Govindarajan and K. C. Sahu, Annu. Rev. Fluid Mech. **46**, 331 (2014).

[64] P. Atsavapranee and M. Gharib, J. Fluid Mech. **342**, 53 (1997).

[65] W. R. Peltier and C. R. Caulfield, Annu. Rev. Fluid Mech. **35**, 135 (2003).

[66] S. Chandrasekhar, *Hydrodynamic and Hydromagnetic Stability* (Clarendon Press, Oxford, 1961).

[67] T. Funada and D. D. Joseph, J. Fluid Mech. **445**, 263 (2001).

[68] I. P. D. De Silva, H. J. S. Fernando, F. Eaton, and D. Hebert, Earth Planet Sci. Lett. **143**, 217 (1996).

[69] D. I. Pullin, J. Fluid Mech. **119**, 507 (1982).

[70] R. D. Moser and M. M. Rogers, J. Fluid Mech. **247**, 275 (1993).
[71] R. Zhang, X. He, G. D. Doolen, and S. Chen, Adv. Water Res. **24**, 461 (2001).
[72] H. G. Lee and J. Kim, Eur. J. Mech. B-Fluid **49**, 77 (2015).
[73] Z. L. Guo, C. G. Zheng, and B. C. Shi, Phys. Fluids **14**, 2007 (2002).
[74] Y. Wang, C. Shu, H. B. Huang, and C. J. Teo, J. Comput. Phys. **280**, 404 (2015).
[75] P. Lallemand and L. S. Luo, Phys. Rev. E **61**, 6546 (2000).